arXiv:1206.2003v1 [cond-mat.mes-hall] 10 Jun 2012

Acoustic phonon-limited mobility in two-dimensional MoS_2: Deformation potential and piezoelectric scattering from first principles

Kristen Kaasbjerg,[1,*] Antti-Pekka Jauho,[2] and Kristian S. Thygesen[2,3]
[1]School of Chemistry, The Sackler Faculty of Exact Sciences, Tel Aviv University, 69978 Tel Aviv, Israel
[2]Center for Nanostructured Graphene (CNG), Department of Micro- and Nanotechnology, DTU Nanotech,
Technical University of Denmark, DK-2800 Kongens Lyngby, Denmark
[3]Center for Atomic-scale Materials Design (CAMD), Department of Physics,
Technical University of Denmark, DK-2800 Kongens Lyngby, Denmark

(Dated: March 7, 2013)

We theoretically study the acoustic phonon-limited mobility in two-dimensional n-doped MoS_2 for temperatures $T < 100$ K and high carrier densities using the Boltzmann equation and first-principles calculations of the electron-phonon interaction. The individual deformation potential and piezoelectric interactions with the acoustic phonons are extracted using a real-space partitioning scheme. Combined with analytical considerations, we find that the piezoelectric interaction in two-dimensional (hexagonal) crystals differs qualitatively from the three-dimensional bulk form. Owing to the specific form of the piezoelectric interaction in 2D, the two coupling mechanisms are found to contribute comparably to carrier scattering throughout the considered temperature range. The calculated mobility for screened electron-phonon interaction shows a nontrivial temperature dependence both above and below the Bloch-Grüneisen temperature. In the low-temperature Bloch-Grüneisen regime the mobility approaches a $\mu \sim T^{-6}$ ($\mu \sim T^{-4}$) behavior for screened (unscreened) electron-phonon interaction. Very high intrinsic mobilities in excess of 10^8 cm^2/V s are predicted for $T < 10$ K and high carrier densities ($n \gtrsim 10^{11}$ cm^{-2}).

PACS numbers: 72.10.-d, 72.80.Jc, 81.05.Hd

I. INTRODUCTION

Two-dimensional (2D) atomic crystals[1] such as graphene[2–4] are promising candidates for future electronic applications. Single-layer MoS_2 belongs to a new family of 2D materials based on transition metal dichalcogenides (MX_2) which have interesting electronic and optical properties.[5–11] Unlike graphene, 2D MoS_2 is a regular semiconductor with a band gap of ∼1.8 eV.[6] In conjunction with the excellent gate control inherent to atomic-thin materials the finite gap makes it a desirable material for various electronic applications. However, in spite of the recent progress in sample fabrication and transport measurements on gated single to few-layer samples,[1,8,10,12–15] little is still known about the intrinsic carrier properties such as factors limiting the achievable mobilities.

Experimentally, the room-temperature mobility of n-type single-layer MoS_2 ranges from ∼1 to ∼200 cm^2 V^{-1} s^{-1} depending on the device structure.[1,8,12,13] The higher value obtained for a top-gated sample where a high-κ gate dielectric was used,[8] is close to the theoretically predicted intrinsic phonon-limited value of 410 cm^2 V^{-1} s^{-1} for the mobility,[16] indicating that impurity scattering can be strongly suppressed by dielectric engineering.[17] Other theoretical studies have addressed different pertaining issues related to the performance of single-layer MoS_2 transistors.[18,19]

One important limiting factor for the carrier mobility of semiconductor-based two-dimensional electron gases (2DEGs) is scattering on the acoustic phonons of the material. At low-temperatures where scattering on optical phonons is suppressed and with weak impurity scattering, this is among the dominating scattering mechanisms.[20] In the low-temperature regime, acoustic phonon-dominated transport manifests itself in a strong change in the temperature dependence of the carrier mobility once the temperature is lowered below the Bloch-Grüneisen (BG) temperature T_{BG} corresponding to the thermal energy of an acoustic phonon required for full backscattering at the Fermi surface. Explicitly, $k_{\mathrm{B}}T_{\mathrm{BG}} = 2\hbar c_\lambda k_F$, where k_F is the Fermi wave vector, c_λ the sound velocity and k_{B} the Boltzmann constant. For heterostructure-based 2DEGs the BG regime is well-known,[21,22] and recently transport in the BG regime has also been studied in graphene both experimentally[23] and theoretically.[24–26]

In a 2DEG the Fermi wave vector k_F scales with the carrier density as $\sqrt{n}$ and the Bloch-Grüneisen temperature acquires a similar density dependence $k_{\mathrm{B}}T_{\mathrm{BG}} = 2\hbar c_\lambda \sqrt{4\pi n/g_s g_v}$ with g_s and g_v denoting the spin and valley degeneracy, respectively.[27] For single-layer MoS_2 ($g_v = 2$) this results in the following BG temperatures

$$T_{\mathrm{BG}}^{\mathrm{TA}} \approx 11\sqrt{n}\,\mathrm{K} \quad \text{and} \quad T_{\mathrm{BG}}^{\mathrm{LA}} \approx 18\sqrt{n}\,\mathrm{K}, \qquad (1)$$

for the transverse (TA) and longitudinal (LA) acoustic phonons, respectively, with the carrier density measured in units of 10^{12} cm^{-2}. These numbers are on the same order of magnitude as those for graphene,[25] and transport in the high-mobility BG regime should be achievable in single-layer MoS_2 (and other 2D transition metal dichalcogenides). However, the above considerations also emphasize the importance of going to high carrier densities $n \gtrsim 10^{12}$ cm^{-2} in order for the BG transition to occur at sufficiently high temperatures where acoustic phonon scattering still dominates over impurity scattering.[20] Indeed, extremely large carrier densities $n \sim 10^{14}$ cm^{-2} have recently been achieved in 2D samples of graphene and MoS$_2$ using advanced electrolytic gating.[10,23]

In the present work, we study the acoustic phonon-limited mobility of n-type 2D MoS$_2$ at low temperatures ($T < 100$ K) taking into account both deformation potential and piezoelectric scattering. In our previous work considering scattering on both acoustic and optical phonons,[16] only the deformation potential interaction was taken into account in the coupling to the acoustic phonons. We stress, however, that since optical phonon scattering dominated the mobility in temperature range ($T > 100$ K) considered in Ref.16, the conclusions reached there are unaffected by the inclusion of piezoelectric scattering. For the temperatures considered in this work, scattering on intrinsic intervalley acoustic/optical phonons is strongly suppressed and can be neglected.[16]

Using a first-principles approach, we here calculate both the deformation potential and piezoelectric interactions in 2D MoS$_2$. Furthermore, an analytic expression for the wave-vector dependence of the piezoelectric interaction in 2D hexagonal crystals is given. This allows us to establish the individual coupling strengths of the two scattering mechanisms. The calculated transport characteristics provide a platform for comparison with future measurements of the carrier mobility in single-layer MoS$_2$ which can (i) lead to an experimental verification of the theoretical deformation potential and piezoelectric couplings reported here,[28] (ii) reveal to which extent the mobility is affected by extrinsic surface acoustic/optical phonons[29,30] which have turned out to be important in graphene samples,[31–33] and (iii) address the importance of the interplay between acoustic phonon and impurity scattering which results in a complex temperature and density dependence of the mobility.[34] In this context previous studies have emphasized the importance of including both the TA and LA phonons in order to obtain good agreement with experiment.[22]

The paper is organized as follows. Section II briefly summarizes the Boltzmann transport theory. In Sec. III the first-principles results for the acoustic electron-phonon interaction are presented and the individual deformation potential and piezoelectric interactions are discussed. Finally, the results for temperature and density dependence of the acoustic phonon-limited mobility are presented in Sec. IV.

II. BOLTZMANN THEORY

Two-dimensional MoS$_2$ has a hexagonal lattice structure like graphene with the bottom of the conduction band residing in the K, K'-points at the corners of the Brillouin zone.[35,36] The two K, K'-valleys are perfectly isotropic and can to a good approximation be described by parabolic bands with an effective mass of $m^* = 0.48\, m_e$.[16]

In Boltzmann theory, the drift mobility $\mu_{xx} = \sigma_{xx}/ne$, where σ_{xx} is the conductivity, is in the presence of (quasi) elastic scattering given by the Drude-like expression[37]

$$\mu_{xx} = \frac{e\langle\tau_k\rangle}{m^*}, \tag{2}$$

where τ_k is the energy-dependent relaxation time and the energy-weighted average $\langle\cdot\rangle$ is defined by

$$\langle A\rangle = \frac{1}{n}\int d\varepsilon_{\mathbf{k}}\, \rho(\varepsilon_{\mathbf{k}})\varepsilon_{\mathbf{k}} A_{\mathbf{k}} \left(-\frac{\partial f}{\partial \varepsilon_{\mathbf{k}}}\right). \tag{3}$$

Here, n is the two-dimensional carrier density, $\rho = g_s g_v m^*/2\pi\hbar^2$ is the density of states in 2D, $\varepsilon_{\mathbf{k}} = \hbar^2k^2/2m^*$ is the carrier energy, and $f(\varepsilon_{\mathbf{k}}) = \{1 + \exp[(\varepsilon_{\mathbf{k}} - E_F)/k_{\mathrm{B}}T]\}^{-1}$ is the equilibrium Fermi-Dirac distribution function. For a degenerate electron gas, only scattering within a thin shell of width $k_{\mathrm{B}}T$ around the Fermi level is relevant and $\mu_{xx} \approx e\tau_{k_F}/m^*$ applies.

In the case of acoustic phonon scattering which to a good approximation can be treated as a quasielastic scattering process, the relaxation time for each of the acoustic phonons is given by[16,37]

$$\frac{1}{\tau_{\mathbf{k}\lambda}} = \sum_{\mathbf{k}'} (1 - \cos\theta_{\mathbf{k},\mathbf{k}'})\, P^{\lambda}_{\mathbf{k}\mathbf{k}'} \frac{1 - f_{\mathbf{k}'}}{1 - f_{\mathbf{k}}}, \tag{4}$$

where λ denotes the acoustic phonon branch index ($\lambda =$TA, LA), $\theta_{\mathbf{k},\mathbf{k}'}$ is the scattering angle and $f_{\mathbf{k}} = f(\varepsilon_{\mathbf{k}})$ is understood. The transition matrix element is given by

$$P^{\lambda}_{\mathbf{k}\mathbf{k}'} = \frac{2\pi}{\hbar}\sum_{\mathbf{q}} \frac{|g^{\lambda}_{\mathbf{k}\mathbf{q}}|^2}{\epsilon^2(q,T)} \Big[N_{\mathbf{q}\lambda}\delta(\varepsilon_{\mathbf{k}'} - \varepsilon_{\mathbf{k}} - \hbar\omega_{\mathbf{q}\lambda}) + (1 + N_{\mathbf{q}\lambda})\,\delta(\varepsilon_{\mathbf{k}'} - \varepsilon_{\mathbf{k}} + \hbar\omega_{\mathbf{q}\lambda})\Big], \tag{5}$$

where $g^{\lambda}_{\mathbf{k}\mathbf{q}}$ is the electron-phonon coupling, $\epsilon(q,T)$ is the wave vector and temperature dependent static dielectric function of the carriers, and $\hbar\omega_{\mathbf{q}\lambda}$ the acoustic phonon energy. The phonons are assumed to be in equilibrium and populated according to the Bose-Einstein distribution function $N_{\mathbf{q}\lambda} = N(\hbar\omega_{\mathbf{q}\lambda})$. Under the assumption of quasielastic scattering, the phonon energies in the δ-functions of Eq. (5) are neglected.

Above the BG temperature where the equipartion approximation $N_{\mathbf{q}} \sim k_{\mathrm{B}}T/\hbar\omega_{\mathbf{q}} \gg 1$ applies and with screening neglected, the relaxation time for acoustic deformation potential scattering is given by the simple expression[16]

$$\frac{1}{\tau_{\mathbf{k}\lambda}} = \frac{m^*\Xi_\lambda^2 k_{\mathrm{B}}T}{\hbar^3\rho c_\lambda^2}, \tag{6}$$

where Ξ_λ is the acoustic deformation potential.[38] Here, the independence on the carrier energy gives rise to a

$\mu \sim T^{-1}$ temperature dependence of the mobility in the high-temperature regime.

The screening of the electron-phonon interaction by the carriers themselves is accounted for at the level of finite-temperature Thomas-Fermi theory where the static dielectric function of the 2DEG is given by

$$\epsilon(q,T) = 1 + \frac{q_{\mathrm{TF}}(T)}{q}, \tag{7}$$

where $q_{\mathrm{TF}}(T)$ is the finite-temperature Thomas-Fermi screening wave vector (see App. A for details).

For the numerical evaluation of the relaxation time in Eq. (4) quasielastic scattering on the acoustic phonons is assumed. It should be stressed that while the phonon energies in the δ-functions of Eq. (5) are omitted, they must be retained in the rapidly varying Fermi functions in Eq. (4). This is particularly important in the BG regime where the phonon energy becomes comparable to the thermal smearing at the Fermi level, i.e. $\hbar\omega_{\mathbf{q}\lambda} \sim k_{\mathrm{B}}T$.

III. INTERACTION WITH ACOUSTIC PHONONS

In the following, the electron-phonon interaction is calculated from first principles using the density-functional based method outlined in Ref.16. The interaction with the acoustic phonons can be written in the general form

$$g_{\mathbf{kq}}^{\lambda} = \sqrt{\frac{\hbar}{2A\rho\omega_{\mathbf{q}\lambda}}} M_{\mathbf{kq}}^{\lambda}, \tag{8}$$

where A is the area of the sample, ρ is the mass density, $M_{\mathbf{kq}}^{\lambda} = \langle \mathbf{k}+\mathbf{q} | \delta V_{\mathbf{q}\lambda} | \mathbf{k} \rangle$ is the matrix element between the Bloch states with wave vectors $\mathbf{k}$ and $\mathbf{k}+\mathbf{q}$, and $\delta V_{\mathbf{q}\lambda}$ is the change in the crystal potential due to a phonon with wave vector $\mathbf{q}$ and branch index λ. The couplings in the K, K' valleys are related through time-reversal symmetry as $|M_{\mathbf{q}\lambda}^{K}| = |M_{-\mathbf{q}\lambda}^{K'}|$. As the hexagonal lattice of two-dimensional MoS_2 lacks a center of symmetry, charge carriers in single-layer MoS_2 interact with acoustic phonons through both the deformation potential and the piezoelectric interaction. The coupling matrix element therefore has contributions from both coupling mechanisms, i.e.

$$M_{\mathbf{q}\lambda} = M_{\mathbf{q}\lambda}^{\mathrm{df}} + M_{\mathbf{q}\lambda}^{\mathrm{pz}}. \tag{9}$$

In three-dimensional bulk crystals, the two coupling mechanisms are most often assumed to be out of phase, i.e. one is real and the other imaginary.[38] This implies that piezoelectric and deformation potential interactions do not interfere in lowest-order perturbation theory, i.e. $|M_{\mathbf{q}\lambda}|^2 = |M_{\mathbf{q}\lambda}^{\mathrm{df}} + M_{\mathbf{q}\lambda}^{\mathrm{pz}}|^2 = |M_{\mathbf{q}\lambda}^{\mathrm{df}}|^2 + |M_{\mathbf{q}\lambda}^{\mathrm{pz}}|^2$.

By noticing that the deformation potential is short-ranged and the piezoelectric interaction long-ranged in nature, we have deviced the real-space partitioning scheme outlined in App. B to separate out the two mechanisms from the total electron-phonon coupling. The couplings to the TA and LA phonons for $\mathbf{k} = \mathbf{K}$ resulting from this partitioning scheme are shown in Fig. 1 with the deformation potential and piezoelectric couplings in the upper and lower row, respectively.[39] While the deformation potential couplings have the three-fold rotational symmetry of the conduction band in the vicinity of the K, K' points of the Brillouin zone, the six-fold rotational symmetry of the piezoelectric couplings originates from the hexagonal crystal lattice. From the first-principles calculation of the total matrix elements (not shown) we find that the above-mentioned out-of-phase property of the two coupling mechanisms only holds for the LA phonon. For the TA phonon the two mechanisms interfere and must hence be considered together.

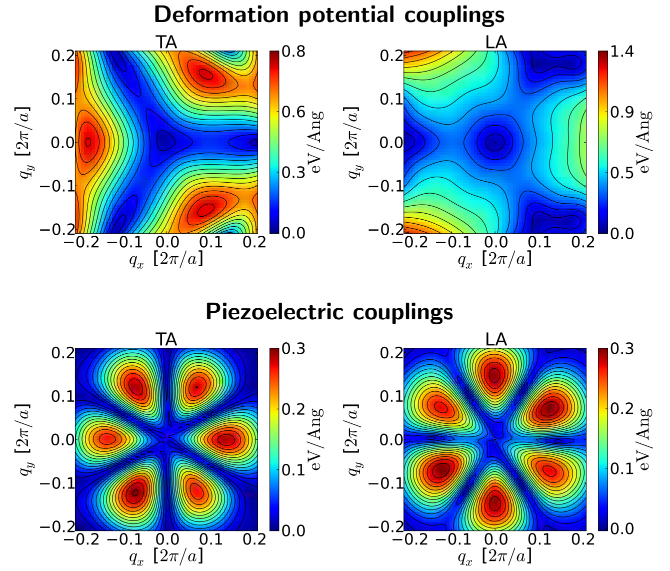

FIG. 1: (Color online) Acoustic electron-phonon couplings in the K-valley of the conduction band in two-dimensional MoS_2. The plots show the absolute value of the first-principles coupling matrix elements $|M_{\mathbf{q}\lambda}^{\mathrm{df/pz}}|$ at $\mathbf{k} = \mathbf{K}$ for the TA and LA phonons as a function of the two-dimensional phonon wave vector $\mathbf{q}$. (Upper row) Deformation potential couplings. (Lower row) Piezoelectric couplings.

In the following two sections the two coupling mechanisms are analyzed in closer detail. Analytic expressions for the couplings are introduced and the coupling strengths are determined from the first-principles electron-phonon couplings.

A. Deformation potential interaction

The origin of the deformation potential interaction lies in the local changes of the crystal potential that accompanies the atomic displacements due to an acoustic phonon. It therefore requires microscopic considerations as the one adopted here to determine the interaction strength.

In the following we adopt the common approach and assume that the deformation potential interaction is isotropic and linear in the phonon wave vector, i.e.

$$|M^{\mathrm{df}}_{\mathbf{q}\lambda}| = \Xi_\lambda q, \tag{10}$$

where Ξ_λ is the acoustic deformation potential.[38] As this is not the case for the *true* deformation potential couplings in Fig. 1 which are anisotropic and show a more complex q-dependence at shorter wavelengths, the deformation potential must be regarded as an *effective* coupling parameter. In valley-degenerate semiconductors where the couplings in the different valleys are related through time-reversal symmetry, the *effective* deformation potential of Eq. (10) can furthermore be regarded as a valley-averaged coupling parameter that implicitly accounts for the variation in the coupling between the different valleys. We will here use the *effective* deformation potentials for the TA and LA phonons from Ref.16 (see Table I).

It should be noted that the first-principles deformation potential couplings contain contributions from umklapp processes, i.e. Fourier components of the crystal potential involving reciprocal lattice vectors $\mathbf{G}$. As umklapp processes are of shorter wavelength ($\mathbf{q}+\mathbf{G}$) compared to the phonon wave vector $\mathbf{q}$, screening of the electron-phonon interaction with $\epsilon(q)$ as done in Eq. (5) can lead to an overscreening of the deformation potential interaction. However, we are at present not able to quantify the relative contributions from normal ($\mathbf{G}=0$) and umklapp processes in further detail. Under the assumption that the former dominates the deformation potential interaction, screening with a long-wavelength dielectric function is legitimate. On the other hand, if umklapp processes dominate, the individual $\mathbf{q}+\mathbf{G}$ contributions to the deformation potential interaction should be screened with the dielectric function evaluated at $\mathbf{q}+\mathbf{G}$.

B. Piezoelectric interaction

Piezoelectric coupling to acoustic phonons occurs in crystals lacking a center of symmetry and originates from the macroscopic polarization that accompanies an applied strain ϵ_{ij}. The strength of the interaction is given by the piezoelectric tensor e_{ij} here given in Voigt notation.

In App. C we provide a derivation of the piezoelectric interaction in 2D materials based on a continuum description. We find that the piezoelectric coupling for a 2D hexagonal crystal is given by

$$|M^{\mathrm{pz}}_{\mathbf{q}\lambda}| = \frac{e_{11}e}{\epsilon_0} q \times \mathrm{erfc}(q\sigma/2)|A_\lambda(\hat{\mathbf{q}})|, \tag{11}$$

where e_{11} (units of C/m) is the only independent component of the piezoelectric tensor of the 2D hexagonal lattice,[40] ϵ_0 is the vacuum permeability, erfc is the complementary error function, σ is an effective width of the electronic wave functions, and $A_\lambda(\hat{\mathbf{q}})$ is an anisotropy factor that accounts for the angular dependence of the piezoelectric interaction. The latter is given by

$$A_{\mathrm{TA}}(\hat{\mathbf{q}}) = \sin^3\theta_{\mathbf{q}} - 3\sin\theta_{\mathbf{q}}\cos^2\theta_{\mathbf{q}}, \tag{12}$$

$$A_{\mathrm{LA}}(\hat{\mathbf{q}}) = \cos^3\theta_{\mathbf{q}} - 3\cos\theta_{\mathbf{q}}\sin^2\theta_{\mathbf{q}} \tag{13}$$

for the TA and LA phonons, respectively,[41] and results in the highly anisotropic piezoelectric interaction shown in the lower panel of Fig. 1. The extrema of the piezoelectric interaction occur along high-symmetry directions of the hexagonal lattice with the directions of minimum coupling to the TA phonon and maximum coupling to the LA phonon, and vice versa, coinciding.

TABLE I: Material parameters for single-layer MoS$_2$ used in the present work. Except for the piezoelectric constant which has been obtained by fitting the analytic result for the piezoelectric interaction in Eq. (11) to the first-principles results in Fig. 1, all parameters have been adopted from Ref.16.

Parameter	Symbol	Value
Lattice constant	a	3.14 Å
Ion mass density	ρ	3.1×10^{-7} g/cm^2
Effective electron mass	m^*	0.48 m_e
Transverse sound velocity	c_{TA}	4.2×10^3 m/s
Longitudinal sound velocity	c_{LA}	6.7×10^3 m/s
Acoustic deformation potentials		
TA	Ξ_{TA}	1.6 eV
LA	Ξ_{LA}	2.8 eV
Piezoelectric constant	e_{11}	3.0×10^{-13} C/cm
Effective layer thickness	σ	4.41 Å

The agreement between Eq. (11) and the first-principles results for the piezoelectric interaction in Fig. 1 is very good (see also Fig. 6 in App. C). Though, for $q < 2\pi/L_{\mathrm{cell}}$, where L_{cell} is the size of the supercell used for the calculation of the electron-phonon interaction, the correct analytic behavior of the first-principles piezoelectric interaction cannot be captured (see App. B). From the first-principles results, the piezoelectric constant of 2D MoS$_2$ is estimated to be $e_{11} \sim 3.0 \times 10^{-13}$ C/cm ($\sim$0.01 e/bohr) which is an order of magnitude smaller than the theoretical value for 2D hexagonal BN obtained with a Berry's phase approach.[40] Similar Berry's phase calculations for 2D MoS$_2$ are required to verify the value predicted here.

The q-dependence of the piezoelectric coupling in Eq. (11) is qualitatively different from the one in 3D bulk systems where $M^{\mathrm{pz}}_{\mathbf{q}\lambda} \sim$ constant.[38] In the long-wavelength limit where $\mathrm{erfc}(q\sigma/2) \sim 1 - q\sigma/\sqrt{2\pi}$, the 2D piezoelectric interaction in Eq. (11) acquires a linear q-dependence $M^{\mathrm{pz}}_{\mathbf{q}\lambda} \sim q$. Hence, there is no qualitative difference between the deformation potential interaction in Eq. (10) and the 2D piezoelectric interaction in the long-wavelength limit. Under the assumption that the linear long-wavelength behavior holds, the high-temperature relaxation time for piezoelectric scattering is given by Eq. (6) with the replacement[42]

$$\Xi_\lambda^2 \to \frac{1}{2}\left(\frac{e_{11}e}{\epsilon_0}\right)^2, \qquad (14)$$

where the factor $1/2 = \langle A_\lambda^2 \rangle$ stems from the angular mean of the piezoelectric interaction. This corresponds to an effective isotropic piezoelectric coupling with $A_\lambda(\hat{\mathbf{q}}) = 1/\sqrt{2}$ in Eq. (11).

Due to the similarity of the deformation potential and piezoelectric interaction in the long-wavelength limit, the relative strength of the two interaction mechanisms is governed by the ratio $(e_{11}e/\epsilon_0)/\Xi_\lambda$ of the prefactors in Eqs. (10) and (11). Since this is on the order of unity with the parameters for $\mathrm{MoS_2}$ listed in Table I, both coupling mechanisms must be considered. Furthermore, due to the interference between the two mechanisms for the TA phonon, the total coupling for the TA phonon differs in the K, K' valleys for a given direction of the carrier wave vector $\mathbf{k}$. The Boltzmann equation must hence be solved explicitly in both valleys and the valley-averaged relaxation time $\tau = (\tau_K + \tau_{K'})/2$, where $\tau_{K/K'}$ denotes the total relaxation time in the individual valleys, must be used in Eq. (2) for the mobility.

IV. RESULTS

In the following we use the Boltzmann equation approach outlined in Section II to study the temperature ($\mu \sim T^{-\gamma}$) and density dependence of the acoustic phonon-limited mobility in the temperature regime $T < 100$ K and for high carrier densities $1 \times 10^{10} - 3 \times 10^{13}\ \mathrm{cm^{-2}}$. The temperature dependence of the resistivity $\rho = (ne\mu)^{-1}$ follows the same power law with a change in the sign of the exponent.

In order to establish the relative strength of deformation potential and piezoelectric scattering in 2D $\mathrm{MoS_2}$ we first consider the two scattering mechanisms separately. Figure 2 shows the calculated inverse momentum relaxation times due to deformation potential (dashed lines) and piezoelectric (full lines) scattering at temperatures $T = 10$ K and $T = 50$ K and a carrier density of $n = 10^{13}\ \mathrm{cm^{-2}}$. This corresponds to a Fermi level of $E_F \sim 25$ meV and BG temperatures of ∼36 K and ∼57 K for the TA and LA phonons, respectively. The dip in the inverse relaxation time at the Fermi level that develops with decreasing temperature is a signature of transport in the BG regime. In this temperature regime the freezing out of short-wavelength acoustic phonons and the sharpening of the Fermi surface strongly limit the phase space available for scattering on acoustic phonons and result in a strong suppression of scattering at the Fermi level. The figure clearly demonstrates that deformation potential and piezoelectric scattering are on the same order of magnitude in two-dimensional $\mathrm{MoS_2}$. At higher energies deformation potential scattering dominates due to the different q-dependencies of the two coupling mechanisms. In the relevant energy range around the Fermi level, the relative strength of the two scattering mechanisms is found to be weakly dependent on the carrier density.

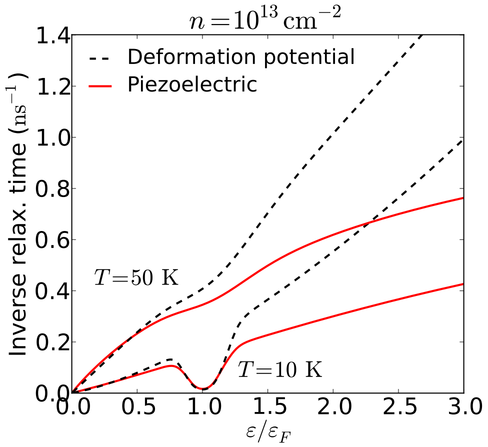

FIG. 2: (Color online) Inverse relaxation time for screened deformation potential (dashed lines) and piezoelectric (full lines) scattering at temperatures $T = 10$ K and $T = 50$ K. The carrier density is $n = 10^{13}\ \mathrm{cm^{-2}}$ corresponding to a Fermi energy of $E_F \approx 25$ meV and a BG temperature of $T_{\mathrm{BG}} \approx 36$ (57) K for the TA (LA) phonon. At $T = 10$ K the dip in the inverse relaxation time at the Fermi energy is a clear fingerprint of Bloch-Grüneisen physics.

Due to the highly anisotropic piezoelectric interaction and its interference with the deformation potential interaction in the coupling to the TA phonon, the mobility in 2D $\mathrm{MoS_2}$ depends on the direction of the applied electric field relative to the orientation of the crystal lattice. However, in the following we shall focus on a single orientation[43] and note that the mobility changes slightly with the field oriented along the other high-symmetry direction of the hexagonal lattice. Along the chosen direction of the applied field, we find that the interference in the coupling to the TA phonon cancels and the deformation potential and piezoelectric interactions can be treated separately.

Before we consider the mobility in the presence of carrier screening, we briefly summarize the temperature dependence of the mobility in the absence of screening. This is relevant at low carrier densities and for deformation potential couplings dominated by umklapp processes where screening by the carriers is less efficient and to a good approximation can be neglected. Above the BG temperature, the relaxation time for deformation potential scattering in Eq. (6) gives rise to a linear ($\gamma = 1$) behavior while piezoelectric scattering produces a slightly sublinear ($\gamma \lesssim 1$) behavior. The total mobility follows the latter. At low temperatures $T \ll T_{\mathrm{BG}}$, we find that the temperature dependence converges towards a $\gamma = 4$ behavior in all cases due to the identical long-wavelength limits of the deformation potential and piezoelectric cou-

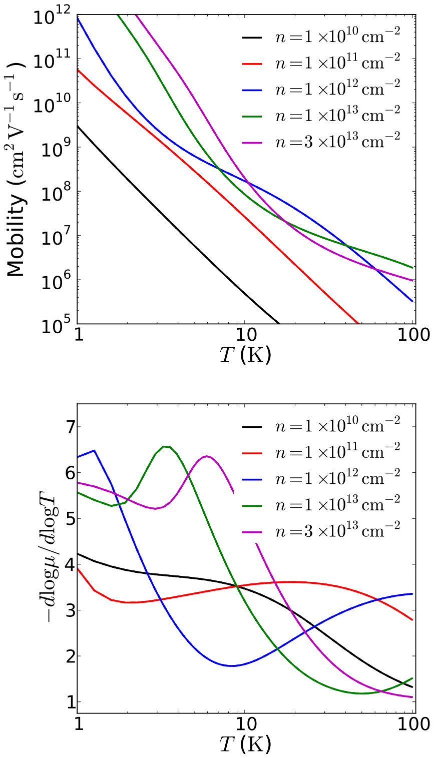

FIG. 3: (Color online) Acoustic phonon-limited mobility vs temperature for screened electron-phonon interaction. (Upper) Mobility vs temperature for different carrier densities. (Lower) Temperature dependence of the exponent γ in $\mu \sim T^{-\gamma}$ for the same set of carrier densities.

plings in Eqs. (10) and (11).

Figure 3 summarizes the temperature dependence of the calculated acoustic phonon-limited mobility for carrier densities $1 \times 10^{10} - 3 \times 10^{13}$ cm^{-2} corresponding to BG temperatures up to ∼62 K (∼99 K) for the TA (LA) phonon. Both the mobility (upper) and the exponent $\gamma = -d \log \mu / d \log T$ of its temperature dependence (lower) are shown. In general, the interplay between BG physics and the quantum-classical crossover from a degenerate to a nondegenerate carrier distribution at $T \sim T_F \approx 29\, n$ K (with n measured in units of 10^{12} cm^{-2}) results in a nontrivial temperature and density dependence of the mobility. At the lowest densities the characteristic temperatures T_{BG} and T_F are comparable while $T_F > T_{\text{BG}}$ for $n \gtrsim 10^{12}$ cm^{-2}. The crossover to the BG regime at $T \sim T_{\text{BG}}$ is therefore more clear for the higher carrier densities.

At temperatures $T \gtrsim T_F$ above the quantum-classical crossover, the mobility shows a $1 \lesssim \gamma \lesssim 4$ dependence for all densities which originates from the temperature dependent the dielectric function. The characteristic nonmonotic behavior of the exponent in this regime shifts to higher temperatures with increasing density. A more correct description of the dielectric function might give rise to minor quantitative modifications of this temperature dependence (see e.g. Ref.34). The unscreened high-temperature behavior $\mu \sim T^{-1}$ of the mobility is only approached for the lowest carrier density in the considered temperature range. The expression $1/\mu = 1/\mu_0 + \alpha T$ often used to fit experimental mobilities,[28] where μ_0 is the residual mobility due to e.g. impurity scattering and α is the density-dependent slope of the temperature dependence, is therefore not expected to apply.

In the low-temperature BG regime $T < T_{\text{BG}}$, a stronger $\gamma \gtrsim 4$ temperature behavior appears. The non-monotonic behavior of the exponent in the BG regime is found to be present also in the absence of screening and can therefore not be attributed to screening effects. As expected from Eq. (1), the characteristic features in the temperature dependence of the exponent also here shift to higher temperatures with increasing density. We find that the mobility approaches a $\gamma = 6$ limiting behavior at $T \ll T_{\text{BG}}$. The same holds for the mobilities due to separate deformation potential and piezoelectric scattering. This is in agreement with the analytic considerations for deformation potential scattering on 2D phonons of Ref.34. Because of the specific form of the piezoelectric interaction derived here and the 2D nature of the phonons, this differs from the usual low-temperature dependence for a 2DEG with scattering on bulk 3D phonons in heterostructures where the temperature dependence is predicted to saturate at $\gamma = 5$ and $\gamma = 7$ for screened piezoelectric and deformation potential interaction, respectively.[21,22] As the calculated low-temperature limits of the mobility are only realized deep inside the BG regime $T \ll T_{\text{BG}}$, they may, however, be of limited practical relevance.

The low-temperature mobilities at $T \lesssim 8$ K show a general increase as a function of the carrier density. At $T \gtrsim 8$ K the change in the screening properties following the quantum-classical crossover makes the density dependence more complicated. The density dependence of the mobility is shown explicitly in Fig. 4 for $T = 4$ K and $T = 20$ K. At densities corresponding to a Fermi temperature $T_F \gtrsim T$ slightly larger than the tempera-

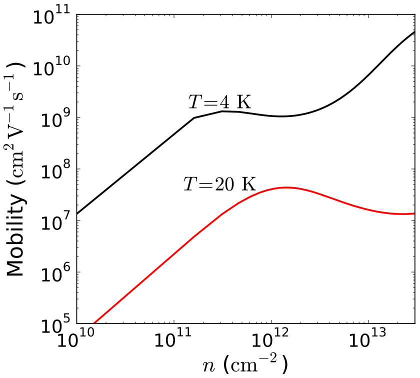

FIG. 4: (Color online) Acoustic phonon-limited mobility vs carrier density for screened electron-phonon interaction and temperatures $T = 4$ K and $T = 20$ K.

ture, the increasing low-density behavior is replaced by a plateau with a slowly decreasing density dependence. Only for degenerate carrier distributions $n \gtrsim 10^{12}$ cm^{-2} at $T = 4$ K is this followed by an increasing density dependence. The increase in the mobility with the carrier density in the degenerate low-temperature regime can be explained by the corresponding increase in the Fermi velocity. Other factors affecting the mobility such as the level of screening and phonon scattering do not vary significantly with the density in this regime. Together with the general high level of screening in 2D MoS$_2$ (see App. A), this results in very high intrinsic mobilities in excess of 10^8 cm^2 V^{-1} s^{-1} at $T < 10$ K and high carrier densities.

V. CONCLUSIONS

In this work we have combined analytic and first-principles calculations of the electron-phonon interaction with a numerical solution of the Boltzmann equation to study the acoustic phonon-limited mobility in 2D MoS$_2$. Our findings are also relevant for the carrier mobility in other 2D piezoelectric materials. The key results are, (i) the analytic expression in Eq. (11) for the piezoelectric interaction in 2D hexagonal materials which is qualitatively different from the one in 3D bulk system and which results in similar temperature dependencies of deformation potential and piezoelectric scattering, (ii) a method to separate out short-range and long-range contributions to the electron-phonon interaction in first-principles calculations, (iii) $\mu \sim T^{-\gamma}$ with $\gamma \sim 6$ (4) at $T \ll T_{\text{BG}}$ for screened (unscreened) electron-phonon interaction, and (iv) an intrinsic mobility that despite the large effective mass ($m^* = 0.48$) of the conduction band in 2D MoS$_2$ increases beyond 10^8 cm^2 V^{-1} s^{-1} at $T < 10$ K and high carrier densities.

Acknowledgments

We thank O. Hod and A. Konar for fruitful discussions. The Center for Nanostructured Graphene is sponsored by the Danish National Research Foundation. This work was supported by the Villum Kann Rasmussen Foundation.

Appendix A: 2D Thomas-Fermi screening

In the Thomas-Fermi (TF) approach to screening, the finite-temperature dielectric function of a 2DEG is in the long-wavelength limit given by

$$\epsilon(q,T) = 1 + \frac{q_{\text{TF}}(T)}{q} \tag{A1}$$

where

$$q_{\text{TF}}(T) = q_{\text{TF}} \left[1 - \exp\left(\frac{-E_F}{k_{\text{B}}T} \right) \right] \tag{A2}$$

is the temperature dependent screening wave vector, $q_{\text{TF}} = e^2/(2\epsilon_0)\rho_0$ the zero-temperature TF wave vector, $\rho_0 = g_s g_v m^*/2\pi\hbar^2$ the constant density of states in 2D, and $E_F = n/\rho_0$ the Fermi level. This reproduces the correct RPA and Debye-Hückel results

$$q_{\text{TF}}(T \to 0) = q_{\text{TF}}, \tag{A3}$$

$$q_{\text{TF}}(T \to \infty) = \frac{ne^2}{2\epsilon_0 k_{\text{B}} T} \tag{A4}$$

for the screening wave vector in the low and high-temperature limits, respectively.

Thomas-Fermi screening suffers from the shortcoming that it overestimates the screening properties of the 2DEG at $q > 2k_F$ where there is no phase space available for screening processes. RPA corrections to the dielectric function are required to cure this problem.[44] However, considering quasi-elastic scattering processes where $q \lesssim 2k_F$, TF theory provides a reasonable approximation to the dielectric function.

Due to the density independence of q_{TF}, zero-temperature screening in 2D decreases with increasing density (Fermi wave vector k_F) when scattering on the full Fermi surface is possible. The screening efficiency is controlled by the dimensionless ratio $q_s = q_{\text{TF}}/k_F$ which in 2D is given by

$$q_s = \frac{(g_s g_v)^{3/2} e^2 m^*}{4\pi\epsilon_0 \hbar^2 \sqrt{4\pi n}}. \tag{A5}$$

For $q_s \gg 1$ all scattering processes at the Fermi surface ($q \lesssim 2k_F$) are strongly screened. In the valley-degenerate conduction band of 2D MoS$_2$, $q_s \approx 2 \times 10^2/\sqrt{n}$ with n measured in units of 10^{12} cm^{-2}. The resulting high level of screening is inherent to valley-degenerate 2D semiconductors with large effective masses.

From the above considerations we conclude that screening in 2D MoS$_2$ is very pronounced and reduces the inverse relaxation time in Eq. (4) by several orders of magnitude for the carrier densities considered here. However, it should be noted that the effect could here be overestimated due to the neglect of the form factor from the z-dependence of the electronic wave functions.[44] First-principles calculations of the RPA response function (see e.g. Ref.45) for 2D MoS$_2$ could help to shed further light on this issue. This is, however, not expected to change the level of screening by orders of magnitude.

Appendix B: Real-space partitioning scheme for separation of the short and long-range part of the electron-phonon interaction

In first-principles calculations of the electron-phonon interaction both short-range (deformation potential) and

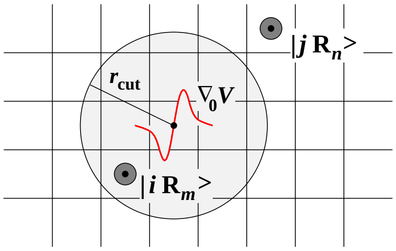

FIG. 5: (Color online) Schematic illustration of the LCAO supercell matrix involved in the calculation of the coupling $M_{\mathbf{kq}}^{\lambda}$ in Eq. (B1). The square lattice indicates the unit cells of the crystal lattice. The real-space cutoff r_{cut} measured from the position of the atomic site where the gradient of the potential is taken, is used to separate out a short-range and a long-range contribution to the coupling matrix element. Matrix elements involving LCAO orbitals located beyond the cutoff as the one shown are defined as long-ranged.

long-range (piezoelectric and Fröhlich interaction) are in general included in the coupling given in Eq. (8). However, due to their different origin it may sometimes be desirable to consider them separately. In the following we provide a real-space partitioning scheme to separate out the short-range and long-range contributions to the coupling matrix element $M_{\mathbf{kq}}^{\lambda}$.

In the present work the electron-phonon interaction has been calculated with an LCAO based supercell method.[16] Within this approach the coupling matrix element due to the phonon-induced change $\delta V_{\mathbf{q}\lambda}$ in the crystal potential is given by

$$\begin{aligned} M_{\mathbf{kq}}^{\lambda} &= \langle \mathbf{k}+\mathbf{q} | \delta V_{\mathbf{q}\lambda}(\mathbf{r}) | \mathbf{k} \rangle \\ &= \frac{1}{N} \sum_{ij} c_i^* c_j \sum_{mn} e^{i\mathbf{k}\cdot(\mathbf{R}_n - \mathbf{R}_m) - i\mathbf{q}\cdot\mathbf{R}_m} \\ &\quad \times \langle i\mathbf{R}_m | \hat{\mathbf{e}}_{\mathbf{q}\lambda} \cdot \nabla_0 V(\mathbf{r}) | j\mathbf{R}_n \rangle, \end{aligned} \tag{B1}$$

where the last equality follows by expanding the Bloch states and phonon-induced change of the potential in an LCAO basis and atomic displacements, respectively, and subsequently exploiting the periodicity of crystal lattice. Here, $|i\mathbf{R}_m\rangle$ denotes an atomic orbital on atom i of the primitive unit cell displaced from a reference cell at $\mathbf{R}_0$ by the lattice vector $\mathbf{R}_m$, c_i is the LCAO expansion coefficients, $\hat{\mathbf{e}}_{\mathbf{q}\lambda}$ is the mass-scaled phonon polarization vector, and $\nabla_0 V$ is the gradient of the crystal potential with respect to atomic displacements in the reference cell.

The central quantity of the partitioning scheme is the LCAO supercell matrix of the atomic gradients in the last line of Eq. (B1). The real-space structure of its matrix elements is illustrated schematically in Fig. 5. The partitioning scheme consists in splitting up the summation in Eq. (B1) into two contributions, (i) a short-ranged part which neglects all matrix elements involving LCAO orbital beyond a chosen real-space cutoff r_{cut}, and (ii) a long-ranged part which includes the remaining matrix elements. In general, the real-space cutoff r_{cut} must be chosen small enough that the short-range part does not include contributions from truly long-range effects in the relevant range of phonon wave vectors, i.e. $\pi/r_{\mathrm{cut}} > q_{\mathrm{max}}$ where q_{max} is the maximum phonon wave vector of interest. At the same time, the cutoff cannot be chosen too small that short-range effects are cut off. The finite real-space range of the electron-phonon interaction inherent to a supercell approach naturally sets a lower limit q_{min} for the magnitude of the phonon wave vector $\mathbf{q}$ at which the long-ranged interactions be obtained reliably. It is given by $q_{\mathrm{min}} = 2\pi/L_{\mathrm{cell}}$ where L_{cell} is the size of the supercell (measured as the diameter of a sphere that can be contained within the supercell).

The real-space partitioning scheme outlined here can be applied in other first-principles calculations of the electron-phonon interaction based on e.g. Wannier functions.[46]

Appendix C: Piezoelectric interaction in 2D hexagonal crystals

Piezoelectric interaction with acoustic phonons appears in crystals which lack a center of symmetry. In this case, the displacement field $u_{\mathbf{q}}(\mathbf{r})$ of the acoustic phonons leads to a polarization $\mathbf{P}$ of the lattice given by[38]

$$P_i = \sum_{jk} e_{i,jk} \epsilon_{jk}, \quad i,j,k = x,y \tag{C1}$$

where

$$\epsilon_{ij} = \frac{1}{2}\left(\frac{\partial u_i}{\partial x_j} + \frac{\partial u_j}{\partial x_i} \right) \tag{C2}$$

is the strain tensor and e is the tensor of piezoelectric moduli having symmetry $e_{i,jk} = e_{i,kj}$. In 2D materials the piezoelectric coupling has units of C/m (C/m^2 in 3D)—the displacement field can be thought to have a normalized z-profile with units of m^{-1}. For a 2D hexagonal lattice with a basis there is only one independent piezoelectric component e_{11} (Voigt notation) which is related to the other nonzero components as[40]

$$e_{11} = -e_{12} = -e_{26}. \tag{C3}$$

Here, the lattice vectors of the hexagonal lattice has been chosen as $\mathbf{a}_{1,2} = a(\sqrt{3}/2, \pm 1/2)$ where a is the lattice constant. For two-dimensional h-BN $e_{11} \sim 10^{-12}$ C/cm.[40]

In the following we derive an analytic expression for the piezoelectric interaction in 2D materials. Considering an isolated 2D material sheet, the in-plane atomic displacements due to an acoustic phonons are in a continuum description represented by the 2D displacement field

$$\mathbf{u}_{\mathbf{q}\lambda}(\mathbf{r}) = \hat{\mathbf{e}}_{\lambda} e^{i\mathbf{q}\cdot\mathbf{r}} f_{\mathbf{q}}(z) Q_{\mathbf{q}\lambda} \tag{C4}$$

where $\mathbf{q} = (q_x, q_y)$ is the two-dimensional phonon wave vector, $\hat{\mathbf{e}}_{\lambda}$ is a unit vector describing the polarization of the phonon λ (to a good approximation independent on

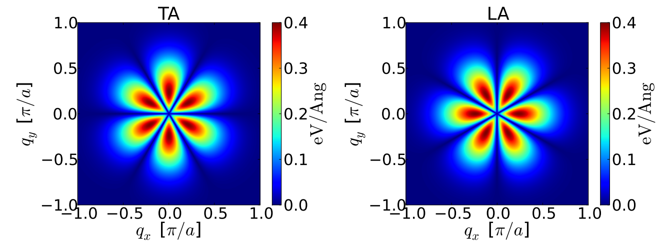

FIG. 6: (Color online) Piezoelectric coupling in a 2D hexagonal crystal. The plots show the absolute value of the coupling matrix element $M_{\text{pz}}^{\lambda}(q)$ in Eq. C15 for the TA (left) and LA (right) phonons as a function of the phonon wave vector $\mathbf{q}$. The parameters for MoS$_2$ in Tab. I have been used.

q in the long-wavelength limit),[38] $f_{\mathbf{q}}$ is the z-profile of the displacement field in the direction perpendicular to the material sheet, and $Q_{\mathbf{q}\lambda} = \sqrt{\hbar/2A\rho\omega_{\mathbf{q}\lambda}}(a_{\mathbf{q}\lambda}^{\dagger} + a_{-\mathbf{q}\lambda})$ is the vibrational normal coordinate. Since we are here interested in the coupling matrix element $M_{\mathbf{kq}}^{\lambda}$ in Eq. (8) the normal coordinate will be left out in the following.

The components of strain tensor follow directly from Eq. (C2) as

$$\epsilon_{xx} = iq_x\hat{e}_{\lambda,x}e^{i\mathbf{q}\cdot\mathbf{r}}f_{\mathbf{q}}(z) \tag{C5}$$

$$\epsilon_{xy} = \epsilon_{yx} = \frac{i}{2}\left(q_y\hat{e}_{\lambda,x} + q_x\hat{e}_{\lambda,y}\right)e^{i\mathbf{q}\cdot\mathbf{r}}f_{\mathbf{q}}(z), \tag{C6}$$

and the associated polarization in Eq. (C1) is given by

$$\begin{aligned} P_{\mathbf{q},x}^{\lambda}(\mathbf{r}) &= e_{11}\left(\epsilon_{xx} - \epsilon_{yy}\right) \\ &= ie_{11}\left(q_x\hat{e}_{\lambda,x} - q_y\hat{e}_{\lambda,y}\right)e^{i\mathbf{q}\cdot\mathbf{r}}f_{\mathbf{q}}(z) \qquad \text{(C7)} \\ P_{\mathbf{q},y}^{\lambda}(\mathbf{r}) &= -2e_{11}\epsilon_{xy} \\ &= -ie_{11}\left(q_y\hat{e}_{\lambda,x} + q_x\hat{e}_{\lambda,y}\right)e^{i\mathbf{q}\cdot\mathbf{r}}f_{\mathbf{q}}(z). \qquad \text{(C8)} \end{aligned}$$

The potential ϕ resulting from the piezoelectric polarization field is given by Poisson's equation $-\epsilon_0\nabla^2\phi(\mathbf{r}) = \rho$ where $\rho = -\nabla\cdot\mathbf{P}$ is the polarization charge. Since we are considering an isolated material sheet, the only boundary condition that applies is $\phi \to 0$ for $z \to \pm\infty$. Fourier transforming in all three directions, we find

$$\epsilon_0(q^2 + k^2)\phi_{\mathbf{q}}(k) = \rho_{\mathbf{q}}f_{\mathbf{q}}(k), \tag{C9}$$

where k is the Fourier variable in the direction perpendicular to the plane of the layer and the Fourier components of the polarization charge are given by

$$\begin{aligned} \rho_{\mathbf{q}\lambda} &= -i\mathbf{q}\cdot\mathbf{P}_{\mathbf{q}}^{\lambda} \\ &= e_{11}\left(q_x^2\hat{e}_{\lambda,x} - q_y^2\hat{e}_{\lambda,x} - 2q_xq_y\hat{e}_{\lambda,y}\right) \\ &\equiv e_{11}q^2A_{\lambda}(\hat{\mathbf{q}}) \qquad \text{(C10)} \end{aligned}$$

where the angular dependencies have been collected in the anisotropy factors A_{λ}. It is given by

$$A_{\text{TA}}(\hat{\mathbf{q}}) = \sin^3\theta_{\mathbf{q}} - 3\sin\theta_{\mathbf{q}}\cos^2\theta_{\mathbf{q}} \tag{C11}$$

$$A_{\text{LA}}(\hat{\mathbf{q}}) = \cos^3\theta_{\mathbf{q}} - 3\cos\theta_{\mathbf{q}}\sin^2\theta_{\mathbf{q}}, \tag{C12}$$

for the TA ($\hat{\mathbf{e}}_{\text{TA}} \perp \mathbf{q}$) and LA ($\hat{\mathbf{e}}_{\text{TA}} \parallel \mathbf{q}$) phonons, respectively.

The z-dependence of the potential is given be the inverse Fourier transform which yields

$$\begin{aligned} \phi_{\mathbf{q}\lambda}(z) &= \frac{e_{11}}{\epsilon_0}A_{\lambda}(\hat{\mathbf{q}})\int dk\, e^{ikz}f_{\mathbf{q}}(k)\frac{q^2}{q^2+k^2} \\ &= \frac{e_{11}}{\epsilon_0}A_{\lambda}(\hat{\mathbf{q}})qe^{-q|z|}, \qquad \text{(C13)} \end{aligned}$$

where in the last equality, a δ-function z-profile with $f_{\mathbf{q}}(k) = 1$ has been assumed. For atomically thin materials, this should be a reasonable approximation.

The coupling matrix element in Eq. (8) follows from the overlap with the envelope $\chi(z)$ of the electronic Bloch functions,

$$M_{\text{pz}}^{\lambda}(q) = \int dz\, \chi^*(z)\phi_{\mathbf{q}\lambda}(z)\chi(z). \tag{C14}$$

Assuming, for simplicity, a Gaussian envelope the long-wavelength limit of the coupling is given by[16]

$$M_{\text{pz}}^{\lambda}(q) = \frac{e_{11}e}{\epsilon_0}q \times \text{erfc}(q\sigma/2)A_{\lambda}(\hat{\mathbf{q}}). \tag{C15}$$

where σ is the effective width of the electronic envelope function. Contrary to the 3D case where the piezoelectric coupling is independent on q,[38] the coupling here depends on the magnitude of the phonon wave vector. The absolute value of the coupling matrix elements are shown in Fig. 6. The six-fold rotational symmetry introduced by the anisotropy factors in Eq. (C11) stems from the hexagonal lattice.

A more detailed treatment of the electronic envelope function is not expected to change the q-dependence of the interaction in Eq. (C15) qualitative. Indeed, the good agreement with our first-principles calculations shown in Fig. 1 confirms this expectation. The introduction of different boundary conditions for the electrostatic potential relevant for e.g. substrate-supported materials sheets is also not expected to change things qualitatively. In any case, the strength of the piezoelectric interaction is given by the piezoelectric constant e_{11} of the material and is not affected by such details.

---

[*] Electronic address: cosby@fys.ku.dk

[1] K. S. Novoselov, D. Jiang, F. Schedin, T. J. Booth, V. V.

Khotkevich, S. V. Morozov, and A. K. Geim, PNAS **102**, 10451 (2005).

[2] A. K. Geim and K. S. Novoselov, Nature Mat. **6**, 183 (2007).

[3] A. H. C. Neto, F. Guinea, N. M. R. Peres, K. S. Novoselov, and A. K. Geim, Rev. Mod. Phys. **81**, 109 (2009).

[4] S. Das Sarma, S. Adam, E. H. Hwang, and E. Rossi, Rev. Mod. Phys. **83**, 407 (2011).

[5] V. Podzorov, M. E. Gershenson, C. Kloc, R. Zeis, and E. Bucher, Appl. Phys. Lett. **84**, 3301 (2004).

[6] K. F. Mak, C. Lee, J. Hone, J. Shan, and T. F. Heinz, Phys. Rev. Lett. **105**, 136805 (2010).

[7] A. Splendiani, L. Sun, Y. Zhang, T. Li, J. Kim, C.-Y. Chim, G. Galli, and F. Wang, Nano. Lett. **10**, 1271 (2010).

[8] B. Radisavljevic, A. Radenovic, J. Brivio, V. Giacometti, and A. Kis, Nature Nano. **6**, 147 (2011).

[9] T. Korn, S. Heydrich, M. Hirmer, J. Schmutzler, and C. Schüller, Appl. Phys. Lett. **99**, 102109 (2011).

[10] Y. Zhang, J. Ye, Y. Matsuhashi, and Y. Iwasa, Nano. Lett. **12**, 1136 (2012).

[11] D. Xiao, G.-B. Liu, W. Feng, X. Xu, and W. Yao, Phys. Rev. Lett. **108**, 196802 (2012).

[12] A. Ayari, E. Cobas, O. Ogundadegbe, and M. S. Fuhrer, J. Appl. Phys. **101**, 014507 (2007).

[13] H. S. S. R. Matte, A. Gomathi, A. K. Manna, D. J. Late, R. Datta, S. K. Pati, and C. N. R. Rao, Angew. Chem. **122**, 4153 (2010).

[14] K.-K. Liu, W. Zhang, Y.-H. Lee, Y.-C. Lin, M.-T. Chang, C.-Y. Su, C.-S. Chang, H. Li, Y. Shi, H. Zhang, et al., Nano. Lett. **12**, 1538 (2012).

[15] H. Liu and P. D. Ye, IEEE Electron Devices Letters **33**, 546 (2012).

[16] K. Kaasbjerg, K. S. Thygesen, and K. W. Jacobsen, Phys. Rev. B **85**, 115317 (2012).

[17] D. Jena and A. Konar, Phys. Rev. Lett. **98**, 136805 (2007).

[18] Y. Yoon, K. Ganapathi, and S. Salahuddin, Nano. Lett. **11**, 3768 (2011).

[19] I. Popov, G. Seifert, and D. Tománek, Phys. Rev. Lett. **108**, 156802 (2012).

[20] E. H. Hwang and S. Das Sarma, Phys. Rev. B **77**, 235437 (2008).

[21] P. J. Price, Solid State Commun. **51**, 607 (1984).

[22] H. L. Stormer, L. N. Pfeiffer, K. W. Baldwin, and K. W. West, Phys. Rev. B **41**, 1278 (1990).

[23] D. K. Efetov and P. Kim, Phys. Rev. Lett. **105**, 256805 (2010).

[24] E. H. Hwang and S. Das Sarma, Phys. Rev. B **77**, 115449 (2008).

[25] E. V. Castro, H. Ochoa, M. I. Katsnelson, R. V. Gorbachev, D. C. Elias, K. S. Novoselov, A. K. Geim, and F. Guinea, Phys. Rev. Lett. **105**, 266601 (2010).

[26] K. Kaasbjerg, K. S. Thygesen, and K. W. Jacobsen, Phys. Rev. B **85**, 165440 (2012).

[27] In a 2DEG the chemical potential is related to the carrier density n via

$$\mu(T) = k_\mathrm{B}T\ln\left(e^{\frac{n}{N_c}}-1\right)$$

where $N_c = g_s g_v m^*/2\pi\hbar^2 k_\mathrm{B}T$ is the effective density of states at the band edge. For the valley-degenerate ($g_v = 2$) conduction band of MoS$_2$, the effective density of states is $N_c \approx 4\times 10^{10}\,T$ cm^{-2} with T measured in K. In the degenerate high-density limit $n \gg N_c$, the Fermi level becomes $E_F \approx 2\pi\hbar^2 n/g_s g_v m^* \sim 2.5\,n$ meV ($k_F = \sqrt{4\pi n/g_s g_v} \sim 0.02\sqrt{n}\,\pi/a$) with n measured in units of 10^{12} cm^{-2}.

[28] T. Kawamura and S. Das Sarma, Phys. Rev. B **42**, 3725 (1990).

[29] A. Knäbchen, Phys. Rev. B **55**, 6701 (1997).

[30] N. Mori and T. Ando, Phys. Rev. B **40**, 6175 (1989).

[31] J.-H. Chen, C. Jang, S. Xiao, M. Ishigami, and M. S. Fuhrer, Nature Nano. **3**, 206 (2008).

[32] S. Fratini and F. Guinea, Phys. Rev. B **77**, 195415 (2008).

[33] A. Konar, T. Fang, and D. Jena, Phys. Rev. B **82**, 115452 (2010).

[34] H. Min, E. H. Hwang, and S. Das Sarma, arXiv:1203.1929 (2012).

[35] S. Lebègue and O. Eriksson, Phys. Rev. B **79**, 115409 (2009).

[36] T. Cheiwchanchamnangij and W. R. L. Lambrecht, Phys. Rev. B **85**, 205302 (2012).

[37] T. Kawamura and S. Das Sarma, Phys. Rev. B **45**, 3612 (1992).

[38] G. D. Mahan, *Many-particle Physics* (Springer, 2010), 3rd ed.

[39] The electron-phonon coupling has been calculated with DFT-LDA using a 17×17 supercell, a double-zeta polarized (DZP) basis for the electronic Bloch states, and 5 Å of vacuum between the MoS$_2$ sheet and the cell boundaries in the direction perpendicular to the sheet. In this direction non-periodic boundary conditions must be applied in order to avoid spurious interlayer contributions to the long-range part of the electron-phonon interaction at long wavelengths (which is present when periodic boundary conditions are applied). A real-space cutoff of $r_\mathrm{cut} = 6.0$ Å has been used to separate out the short-range deformation potential and long-range piezoelectric interactions. We have verified that the results do not change markedly with small changes in the cutoff. Indeed, the calculated deformation potential couplings do not differ significantly from those of Ref.16 where a larger cutoff was used.

[40] N. Sai and E. J. Mele, Phys. Rev. B **68**, 241405 (2003).

[41] The angular dependencies of the matrix elements for the TA and LA phonons in Eqs. (12) and (13) are interchanged compared to the ones in Fig. 1 due to a different orientation of the crystal in the first-principles calculations.

[42] Ideally, this only holds for $\mathbf{k}$ oriented along high-symmetry directions of the hexagonal lattice where $|A_\lambda|^2$ is and even function of $\theta_{\mathbf{k},\mathbf{k}'}$ such that the angular integration of the $\cos\theta_{\mathbf{k},\mathbf{k}'}$ factor in Eq. (4) vanishes.

[43] The field is here applied in the direction of the in-plane projection of the Mo-S bonds.

[44] T. Ando, A. B. Fowler, and F. Stern, Rev. Mod. Phys. **54**, 437 (1982).

[45] J. Yan, J. J. Mortensen, K. W. Jacobsen, and K. S. Thygesen, Phys. Rev. B **83**, 245122 (2011).

[46] F. Giustino, M. L. Cohen, and S. G. Louie, Phys. Rev. B **76**, 165108 (2007).